Wider look at the gravitational-wave transients from GWTC-1 using an unmodeled reconstruction method

Salemi, F ; Milotti, E ; Prodi, G A ; Vedovato, G ; Lazzaro, C ; Tiwari, S ; Vinciguerra, S ; Drago, M ; Klimenko, S

Abstract: In this paper, we investigate the morphology of the events from the GWTC-1 catalog of compact binary coalescences as reconstructed by a method based on coherent excess power: we use an open-source version of the coherent WaveBurst (cWB) analysis pipeline, which does not make use of waveform models. The coherent response of the LIGO-Virgo network of detectors is estimated by using loose bounds on the duration and bandwidth of the signal. This pipeline version reproduces the same results that are reported for cWB in recent publications by the LIGO and Virgo collaborations. In particular, the sky localization and waveform reconstruction are in a good agreement with those produced by methods which exploit the detailed theoretical knowledge of the expected waveform for compact binary coalescences. However, in some cases cWB also detects features in excess in well-localized regions of the time-frequency plane. Here we focus on such deviations and present the methods devised to assess their significance. Out of the 11 events reported in the GWTC-1, in two cases—GW151012 and GW151226—cWB detects an excess of coherent energy after the coalescence (Δt 0.2 and 0.1 s, respectively) with p-values that call for further investigations (0.004 and 0.03, respectively), though they are not sufficient to exclude noise fluctuations. We discuss the morphological properties and plausible interpretations of these features. In case they are genuine, we anticipate that several more such outliers will be uncovered by our methodology in the ongoing advanced LIGO-Virgo observation run (O3).

DOI: https://doi.org/10.1103/physrevd.100.042003

Wider look at the gravitational-wave transients from GWTC-1 using an unmodeled reconstruction method

F. Salemi,[1] E. Milotti,[2] G. A. Prodi,[3,4] G. Vedovato,[5] C. Lazzaro,[6] S. Tiwari,[7] S. Vinciguerra,[1] M. Drago,[6,8] and S. Klimenko[9]

[1]*Albert-Einstein-Institut, Max-Planck-Institut für Gravitationsphysik, D-30167 Hannover, Germany*
[2]*Dipartimento di Fisica, Università di Trieste and INFN Sezione di Trieste, Via Valerio, 2, I-34127 Trieste, Italy*
[3]*Università di Trento, Dipartimento di Fisica, I-38123 Povo, Trento, Italy*
[4]*INFN, Trento Institute for Fundamental Physics and Applications, I-38123 Povo, Trento, Italy*
[5]*INFN, Sezione di Padova, I-35131 Padova, Italy*
[6]*Gran Sasso Science Institute, Via F. Crispi 7, I-67100, L'Aquila, Italy*
[7]*Physik-Institut, University of Zurich, Winterthurerstrasse 190, 8057 Zurich, Switzerland*
[8]*INFN, Laboratori Nazionali del Gran Sasso, I-67100 Assergi, Italy*
[9]*University of Florida, Gainesville, Florida 32611, USA*

(Received 4 June 2019; published 28 August 2019)

In this paper, we investigate the morphology of the events from the GWTC-1 catalog of compact binary coalescences as reconstructed by a method based on coherent excess power: we use an open-source version of the coherent WaveBurst (cWB) analysis pipeline, which does not make use of waveform models. The coherent response of the LIGO-Virgo network of detectors is estimated by using loose bounds on the duration and bandwidth of the signal. This pipeline version reproduces the same results that are reported for cWB in recent publications by the LIGO and Virgo collaborations. In particular, the sky localization and waveform reconstruction are in a good agreement with those produced by methods which exploit the detailed theoretical knowledge of the expected waveform for compact binary coalescences. However, in some cases cWB also detects features in excess in well-localized regions of the time-frequency plane. Here we focus on such deviations and present the methods devised to assess their significance. Out of the 11 events reported in the GWTC-1, in two cases—GW151012 and GW151226—cWB detects an excess of coherent energy after the coalescence ($\Delta t \simeq 0.2$ and $\simeq 0.1$ s, respectively) with p-values that call for further investigations (0.004 and 0.03, respectively), though they are not sufficient to exclude noise fluctuations. We discuss the morphological properties and plausible interpretations of these features. In case they are genuine, we anticipate that several more such outliers will be uncovered by our methodology in the ongoing advanced LIGO-Virgo observation run (O3).

DOI: 10.1103/PhysRevD.100.042003

I. INTRODUCTION

Gravitational-wave (GW) astrophysics is successfully gearing up and is producing a wealth of landmark results, such as the gravitational-wave transient catalog (GWTC-1) of compact binary coalescences (CBC) [1] and the tests of gravity in previously inaccessible regimes [2], from the recent observing runs of the Advanced LIGO [3] and Advanced Virgo [4] detectors. These important achievements come in large part from Bayesian inference applied to template-based methods [5,6]. In particular, these analyses are unveiling the intrinsic properties of the binary black hole mergers, such as masses and spins, thanks to their well-understood theoretical models and their clearly recognizable waveforms (see, e.g., [7–9]).

In our work, we investigate the morphology of the events from the GWTC-1 catalog of compact binary coalescences as reconstructed by an alternative approach that does not depend on specific models, but rather extracts the coherent response of the detector network to generic gravitational waves and uses very loose additional bounds on the duration and bandwidth of the signal. This methodology is robust with respect to a variety of well-known CBC signal features including the higher order modes [10], high mass ratios, misaligned spins and eccentric orbits: it complements the existing template-based algorithms by searching for new and possibly unexpected CBC populations and waveform features. The present analysis extends the well-established analyses reported in [1,2] by looking for features that add to the conventional CBC signal models, especially at times after coalescence.

In Sec. II A, we briefly introduce coherent WaveBurst (cWB), an unmodeled algorithm for searching and reconstructing GW transients and its open source version[1] which is adopted for the production of all results reported in this paper. Section II B describes the Monte Carlo simulation which enables a quantitative evaluation of the consistency between the waveform estimates by cWB versus posterior samples from template-based Bayesian inference. Section III illustrates the actual cWB results for the set of GW events from the GWTC-1 [1][2] and provides the comparison of reconstructed waveforms and sky localizations to those provided by methods based on signal templates. Follow-up studies on the two main outliers (the events GW151012 and GW151226), where cWB detects an excess of coherent energy after coalescence, are reported in Sec. III C. Finally, in Sec. IV we discuss plausible interpretations for the observed deviations in the reconstructed waveforms for GW151012 and for GW151226. We conclude the paper with a very brief discussion of the perspectives for further studies that are enabled by our methods and of the opportunities of their implementation in the ongoing LIGO-Virgo survey [12].

II. METHODS

The primary aim of the paper is to provide a robust method to compare the cWB unmodeled reconstruction with a template-based Bayesian inference. The latter is assumed to be correct and with minimal variance. For each event in the GWTC-1 catalog, we compare the on-source cWB result against a reference distribution built from repetitions of the same experiment. For this Monte Carlo simulation we extract the waveforms from posterior distributions obtained with a template-based analysis and we inject them off source thousands of times.

A. Coherent WaveBurst

Coherent WaveBurst [13] is an analysis pipeline used in searches for generic transient signals with networks of GW detectors. Designed to operate without a specific waveform model, cWB first identifies coincident excess power in the multiresolution time-frequency (TF) representations of the detectors' strain data. It then reconstructs events which are coherent in multiple detectors as well as the source sky location and signal waveform: by using the constrained maximum likelihood method [14], it combines all data streams into one coherent statistic η_c, which is then used for ranking cWB events. This statistic is based on the coherent energy E_C, such that $\eta_c \propto \sqrt{E_C}$, and it is proportional to the coherent signal-to-noise ratio (SNR) in the detector network. To be robust against the nonstationary detector noise, cWB employs signal independent vetoes, which reduce the initial high rate of the excess power triggers. The cWB primary veto cut is on the network correlation coefficient $\mathrm{cc} = E_C/(E_C + E_N)$, where E_N is the residual noise energy, estimated once the reconstructed signal is subtracted from the data [14]. Typically, for a GW signal $\mathrm{cc} \approx 1$ and for instrumental glitches $\mathrm{cc} \ll 1$. Therefore, events with $\mathrm{cc} < 0.7$ are usually rejected as potential glitches. Finally, we used the cWB pipeline configuration with the improved detection efficiency for stellar mass BBH sources. The cWB run parameters were set to select events with the TF patterns where frequency increases with time, which captures the phenomenological behavior of generic CBC chirping signals.

All results reported in this paper have been produced by the open source version 6.3.0 of cWB: this version has been publicly released for open use and it reproduces cWB scientific results included in the most recent publications of the LIGO-Virgo Collaboration based on the observing runs 1 and 2 [1,15–17]. The pipeline and production parameters are the same as in the above-mentioned publications with minimal changes in the code to enable the measurement of quantities needed for the Monte Carlo simulation. While cWB can work with arbitrary detector networks, the waveform reconstruction has been restricted to the Hanford and Livingston detectors, due to the limited contribution by Virgo data to the morphological reconstruction of the events; Virgo data were included instead whenever possible in the sky localization reported in Table III.

B. Monte Carlo simulation methodology

The Monte Carlo simulation described in this section provides the quantitative evaluation of the consistency between the waveform estimates by cWB versus the distribution of waveform posterior samples from template-based Bayesian inference. This method is an evolution of what was already used to estimate the uncertainty on the reconstructed waveforms in Sec. IV of the GWTC-1 catalog paper [1]. We use the same public parameter estimation samples by LALInference [5], released for GWTC-1. For each GW event, we repeatedly add to the actual data stream a waveform extracted at random from the parameter estimation posteriors and perform the signal injection in an off-source period close to the selected event. Next, for each such injection we perform an unmodeled reconstruction and determine the maximum likelihood pointlike estimated waveform and the full likelihood sky map. The final result of the Monte Carlo simulation is an empirical distribution of cWB waveform reconstructions, which is marginalized with respect to the selected parameter estimation posteriors (in this case, with respect to LALInference parameter estimations) and which includes all effects due to non-Gaussian noise fluctuations as well as all biases due to cWB estimation itself. These distributions of waveform and sky localization reconstructions allow the

[1]cWB home page, https://gwburst.gitlab.io/; public repositories, https://gitlab.com/gwburst/public; documentation, https://gwburst.gitlab.io/documentation/latest/html/index.html.

[2]The LIGO-Virgo data are publicly available at the Gravitational Wave Open Science Center [11]; the LIGO-Virgo release of waveform posterior samples is at https://dcc.ligo.org/LIGO-P1800370/public.

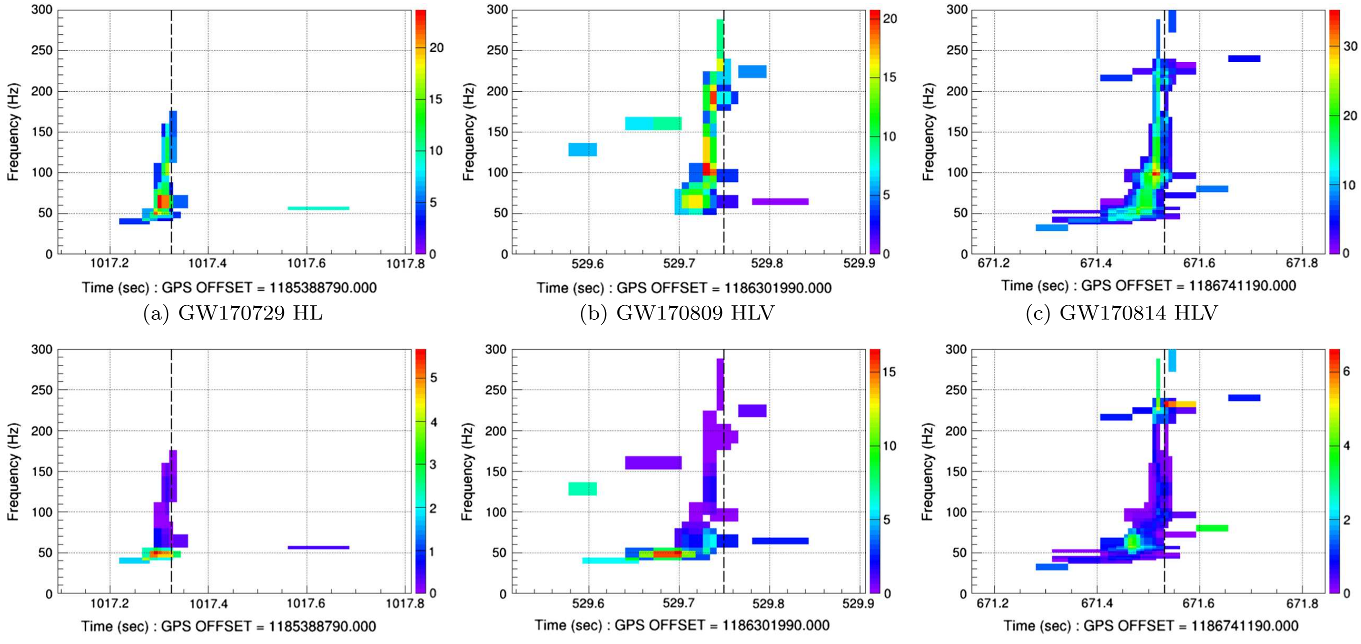

(a) GW170729 HL (b) GW170809 HLV (c) GW170814 HLV

(d) GW170729 HL (e) GW170809 HLV (f) GW170814 HLV

FIG. 1. cWB waveform reconstruction of GW170729, GW170809 and GW170814 in the form of color-coded TF maps. The upper row shows the squared coherent network SNR, while the lower row shows the normalized residual noise energy, E_N, estimated after the reconstructed signal is subtracted from the data. The first column [(a) and (d)] refers to GW170729; next, the second column [(b) and (e)] shows event GW170809; finally, the third column [(c) and (f)] shows the event GW170814. The dashed vertical lines denote the minR $t_{\mathrm{L,coa}}$ for these three events (the network reconstruction uses the Livingston detector time as a reference).

estimation of frequentist confidence intervals and the likelihood sky map coverage. For more details on the actual implementation of the Monte Carlo simulation, see the Appendix B.

III. RESULTS

The Advanced LIGO [3] detectors started taking data on September 12, 2015 until January 19, 2016. This run is referred to as O1. The Advanced LIGO detectors started their second run, called O2, on November 30, 2016, and on August 1, 2017 the Advanced Virgo [4] detector joined the observing run, enabling the first three-detector observations of GWs. This second run ended on August 25, 2017. During the first and the second runs, the LIGO-Virgo searches for binary mergers (both those with matched filters and unmodeled) identified a total of ten BBH mergers and one binary neutron star (BNS) signal. All relevant information on those GW events can be found in the Gravitational-Wave Transient Catalog of Compact Binary Mergers (GWTC-1) [1] and in a number of other papers dedicated to individual GW events [15–20]. Moreover, information on O1 GW events, including a large set of subthreshold candidates, can be found in [21]. Finally, previous tests checking for deviations from CBC models have been discussed in [2].

When considering cWB reconstruction of the 11 main events from the GWTC-1, a subset (i.e., GW151012, GW151226, GW170729, GW170809 and GW170814) displays features in well-localized regions of the TF representation, mainly close to the merger time, which are missing in the usual CBC waveforms [see Fig. 1, Figs. 3(a) and 3(d) and Figs. 5(a) and (d)].

A. cWB unmodeled reconstruction of the events within GWTC–1

For each GW event, we compared the cWB sky localization likelihood map with the corresponding posterior probability sky regions produced by LALInference [5]: while the unmodeled reconstruction produces more extended and irregular sky regions and different biases may arise,[3] the overall overlap between the estimates by cWB and LALInference is mostly good. More details can be found in Appendix A, in particular in Table III and in Fig. 7.

Similarly, for each GW event, the waveforms reconstructed by cWB are compared with those reconstructed from the Monte Carlo simulation which uses LALInference posterior samples: as expected from an algorithm based on excess power, the merger part of the signal is usually well estimated by cWB, while the early inspiral and the

[3]cWB customarily employs an antenna pattern prior, which overweights favorable incoming directions, while underweighting the ones with a poor antenna pattern. This affects especially two-detector networks, as it is the case for this work.

TABLE I. Significance of postcoalescence deviations reconstructed by cWB on the 11 GW events from GWTC-1. For each event we report the following: off-source and on-source average fitting factors, FF, with 1σ uncertainties; the on-source FF corresponding to the minimal residual energy posterior sample; the coherent network SNR as estimated by cWB; the postcoalescence SNR, $\mathrm{SNR}_{\mathrm{pc}}^{\mathrm{minR}}$, assuming the t_{coa} from the minR posterior sample (while $\mathrm{SNR}_{\mathrm{pc}}^{\mathrm{sup}}$ and $\mathrm{SNR}_{\mathrm{pc}}^{\mathrm{inf}}$ are the on-source $\mathrm{SNR}_{\mathrm{pc}}$ corresponding to $\langle t_{\mathrm{coa}}\rangle \pm 2\sigma$, respectively); and finally, the empirically estimated probability that such a $\mathrm{SNR}_{\mathrm{pc}}^{\mathrm{minR}}$ may be produced by a noise fluctuation (where the P_{sup} and P_{inf} values refer to the probability of $\mathrm{SNR}_{\mathrm{pc}}^{\mathrm{inf}}$ and $\mathrm{SNR}_{\mathrm{pc}}^{\mathrm{sup}}$, respectively).

GW event	Source	$\langle\mathrm{FF}\rangle_{\mathrm{offsource}}$	$\langle\mathrm{FF}\rangle_{\mathrm{onsource}}$	$\mathrm{FF}^{\mathrm{minR}}$	SNR	$\mathrm{SNR}_{\mathrm{pc}}^{\mathrm{minR}}\{^{\mathrm{SNR}_{\mathrm{pc}}^{\mathrm{sup}}}_{\mathrm{SNR}_{\mathrm{pc}}^{\mathrm{inf}}}\}$	$\text{p-value}_{\mathrm{pc}}\{^{P_{\mathrm{sup}}}_{P_{\mathrm{inf}}}\}$
GW150914	BBH	0.95 ± 0.02	0.96 ± 0.01	0.97	25.2	$5.72^{6.92}_{5.64}$	$0.94 \pm 0.02^{0.95}_{0.71}$
GW151012	BBH	0.80 ± 0.10	0.82 ± 0.038	0.9	10.5	$6.60^{6.54}_{6.26}$	$0.0037 \pm 0.0014^{0.0068}_{0.0042}$
GW151226	BBH	0.78 ± 0.08	0.75 ± 0.05	0.85	11.9	$4.40^{4.41}_{4.36}$	$0.025 \pm 0.005^{0.03}_{0.02}$
GW170104	BBH	0.90 ± 0.05	0.95 ± 0.03	0.97	13.0	$5.29^{5.30}_{3.95}$	$0.07 \pm 0.01^{0.31}_{0.07}$
GW170608	BBH	0.79 ± 0.07	0.81 ± 0.02	0.84	14.1	$1.69^{1.75}_{1.64}$	$0.51 \pm 0.02^{0.54}_{0.49}$
GW170729	BBH	0.90 ± 0.05	0.93 ± 0.02	0.95	10.2	$4.81^{4.86}_{3.43}$	$0.09 \pm 0.01^{0.35}_{0.08}$
GW170809	BBH	0.90 ± 0.04	0.78 ± 0.03	0.82	11.9	$3.89^{4.71}_{3.88}$	$0.28 \pm 0.01^{0.28}_{0.11}$
GW170814	BBH	0.92 ± 0.03	0.91 ± 0.02	0.93	17.2	$5.98^{6.02}_{5.94}$	$0.10 \pm 0.01^{0.11}_{0.09}$
GW170817	BNS	0.78 ± 0.05	0.7596 ± 0.0004	0.76	29.3	$0.21^{0.21}_{0.21}$	$0.55 \pm 0.01^{0.56}_{0.55}$
GW170818	BBH	0.89 ± 0.06	0.87 ± 0.01	0.92	8.6	$1.97^{2.04}_{1.76}$	$0.87 \pm 0.02^{0.91}_{0.86}$
GW170823	BBH	0.91 ± 0.05	0.96 ± 0.03	0.98	10.8	$3.11^{3.54}_{2.69}$	$0.60 \pm 0.02^{0.74}_{0.44}$

ringdown parts (where the signals are weaker and spread over larger areas in the TF plane) are often missing.

We define the CBC whitened waveforms, $\mathbf{w} = \{w_k(t)\}$, where the index k points to the kth interferometer site, and which are obtained by dividing in the frequency domain the CBC modeled strain waveforms $\mathbf{h} = \{h_k(t)\}$, by the cWB-estimated noise spectral densities, $\sqrt{S_{n,k}(f)}$. We use the notation $\hat{\mathbf{w}}$ to denote the model-independent whitened waveforms reconstructed by cWB, and we define the *fitting factor* of $\hat{\mathbf{w}}$ with respect to $\mathbf{w}$ as

$$\mathrm{FF}(\mathbf{w}, \hat{\mathbf{w}}) = \frac{(\mathbf{w}|\hat{\mathbf{w}})_{\mathbf{t}_1}^{\mathbf{t}_{\mathrm{coa}}}}{\sqrt{(\mathbf{w}|\mathbf{w})_{\mathbf{t}_1}^{\mathbf{t}_{\mathrm{coa}}}}\sqrt{(\hat{\mathbf{w}}|\hat{\mathbf{w}})_{\mathbf{t}_1}^{\mathbf{t}_{\mathrm{coa}}}}}, \tag{1}$$

where the scalar product $(.|.)_{\mathbf{t}_1}^{\mathbf{t}_2}$ is defined in the time domain as

$$(\mathbf{w}|\hat{\mathbf{w}})_{\mathbf{t}_1}^{\mathbf{t}_2} = \sum_k \int_{t_{1,k}}^{t_{2,k}} w_k(t)\hat{w}_k(t)dt, \tag{2}$$

with the index k running over the interferometer sites (i.e., for this paper, Hanford and Livingston in the observing runs O1 and O2). In Eq. (1), $\mathbf{t}_{\mathrm{coa}} = \{t_{\mathrm{coa},k}\}$ is the set of coalescence times as observed in the frame of the kth interferometer.[4] The lower limit of the integration interval, $\mathbf{t}_1 = \{t_{1,k}\}$, is defined by

$$(\hat{\mathbf{w}}|\hat{\mathbf{w}})_{\mathbf{t}_1}^{\infty} = 0.01(\hat{\mathbf{w}}|\hat{\mathbf{w}})_{-\infty}^{\infty}, \tag{3}$$

in practice, the time that sets the lower 1% of the estimated energy of the signal (taking into account the respective time delays between interferometers).

In Table I, we report the average $\langle\mathrm{FF}\rangle_{\mathrm{offsource}}$ calculated by Monte Carlo sampling, where for each injected LALInference posterior $\mathbf{h}^i(t)$ (the index i runs over all posterior samples; see Appendix B for more details), we calculated $\mathrm{FF}(\mathbf{w}^i(t), \hat{\mathbf{w}}^i(t))$, as well as the "on-source" average FF, i.e., $\langle\mathrm{FF}\rangle_{\mathrm{onsource}} = \langle\mathrm{FF}(\mathbf{w}^i(t), \hat{\mathbf{w}}^{\mathrm{gw}}(t))\rangle_i$, where $\hat{\mathbf{w}}^{\mathrm{gw}}(t)$ is the actual cWB whitened waveform of the GW event.

By defining the residual energy of $\hat{\mathbf{w}}^{\mathrm{gw}}$ with respect to the ith CBC whitened sample $\mathbf{w}^i$ as

$$E_{\mathrm{res}}^i = (\mathbf{w}^i - \hat{\mathbf{w}}^{\mathrm{gw}}|\mathbf{w}^i - \hat{\mathbf{w}}^{\mathrm{gw}})_{\mathbf{t}_1}^{\mathbf{t}_2} \tag{4}$$

where

$$(\hat{\mathbf{w}}^{\mathrm{gw}}|\hat{\mathbf{w}}^{\mathrm{gw}})_{-\infty}^{\mathbf{t}_1} = (\hat{\mathbf{w}}^{\mathrm{gw}}|\hat{\mathbf{w}}^{\mathrm{gw}})_{\mathbf{t}_2}^{\infty} = 0.02(\hat{\mathbf{w}}^{\mathrm{gw}}|\hat{\mathbf{w}}^{\mathrm{gw}})_{-\infty}^{\infty}, \tag{5}$$

we can then calculate the sample i corresponding to $\min_i(E_{\mathrm{res}}^i)$ and denote it as the minimal residual energy posterior sample, minR.

The relatively high $\langle\mathrm{FF}\rangle_{\mathrm{offsource}}$ values reported in Table I suggest that cWB is good at reconstructing the injected waveforms before coalescence time. Moreover, from the comparison of the on-source and off-source FFs, we note that there are no significant differences between the two cases and we infer a qualitative compatibility between estimates, with the exception of GW170809, which we shall investigate further in the future.

[4] In this article, we considered just the IMRPhenomP waveform family, where the t_{coa} is the estimated time (with a stationary phase approximation) corresponding to the f_{peak} as defined in Eq. (20) in [8].

B. Significance of postcoalescence excesses

A number of cWB excesses with respect to the CBC templates occur after the coalescence, where CBC waveforms are mostly silent. In order to estimate their significance, we devised a procedure based on their coherent network SNR. We considered the coalescence time, i.e., t_{coa}, as a reference time to start integrating our excesses: we then split our reconstructed waveforms in a *primary* part (i.e., for $t \leq t_{\mathrm{coa}}$) and a *secondary* part (i.e., for $t > t_{\mathrm{coa}}$). Our main test-statistic for the secondary is then the postcoalescence signal-to-noise ratio[5]:

$$\mathrm{SNR}_{\mathrm{pc}} = \sqrt{(\hat{\mathbf{w}}|\hat{\mathbf{w}})^{+\infty}_{\mathbf{t}_{\mathrm{coa}}}}. \tag{6}$$

While for the off-source Monte Carlo simulations, the $\{t_{\mathrm{coa},k}\}$ are known from the CBC posterior samples, for the on-source they can only be estimated, leaving a margin for uncertainty on the on-source SNR_{pc}. We decided to adopt $t_{\mathrm{coa}}^{\mathrm{minR}}$, i.e., the coalescence time of the minimal residual energy CBC posterior sample (already defined in Sec. [1]) as our best point estimate. In Table I, we report the $\mathrm{SNR}_{\mathrm{pc}}^{\mathrm{minR}}$, together with the upper and lower bounds, $\mathrm{SNR}_{\mathrm{pc}}^{\mathrm{sup}}$ and $\mathrm{SNR}_{\mathrm{pc}}^{\mathrm{inf}}$ which correspond to $\langle t_{\mathrm{coa}} \rangle \pm 2\sigma$. Finally, in the last column of Table I, we report the estimated p-value for the on-source coherent SNR excess as the ratio of the number of off-source reconstructed waveforms with a larger or equal value of coherent $\mathrm{SNR}_{\mathrm{pc}}$ over the total number of Monte Carlo reconstructed injections. Consistently with the definition of 2σ SNR upper and lower bounds, we report the upper and lower bounds for the p-value. In order to evaluate the result in the context of multiple hypothesis tests, i.e. when testing multiple null hypotheses, we adopt the concept of "false discovery rate" (FDR) [22] to control the proportion of wrong rejections of the null hypothesis in the set of all "discoveries" [23]: the result is shown in Fig. 2 where the sorted postcoalescence p-values (black dots represent the minR p-values, while the blue and light green vertical lines show the 1 and 2σ [P_{sup}-P_{inf}] bounds, respectively) are plotted against the ranking probability (rank/N_{events}) and compared with a FDR light green dashed area (with an expected fraction of false discoveries $\alpha = 0.1$). Out of the 11 GW events, the postcoalescence p-value$_{\mathrm{pc}}$ for GW151012 is an outlier. The second ranked event, GW151226, though mildly significant, is consistent with the 11 trials.

C. Follow-ups on GW151012 and GW151226

The original reconstruction of GW151012 reveals a primary part consistent with the TF evolution estimated by LALInference, followed by a secondary part, with a chirping structure, at roughly 200 ms after the merger of GW151012, as shown in Fig. 3(a). The E_N in Fig. 3(d) shows that the secondary part, when reconstructed together with the primary, has some relatively high residuals. In order to produce the plots in the second and third columns of Fig. 3, we applied *ad hoc* time vetoes to reconstruct independently the primary [3(b) and 3(e)] and secondary [3(c) and 3(f)] parts. As we see from Fig. 4(a), the estimated sky localizations differ substantially between the primary (blue) and the secondary (green) events, when reconstructed independently, the main reason being the reconstructed time delay between the detectors [Fig. 4(b)]. This suggests that the primary and secondary events might be unrelated.

A similar follow-up analysis was conducted also on GW151226. In Fig. 5(a) and 5(d) the secondary is visible about 100 ms after coalescence. The plots in the second and third columns of Fig. 5 show the primary [5(b) and 5(e)] and secondary [5(c) and 5(f)] events reconstructed independently of one another, the latter being very weak and lacking any structure. Figures 6(a) and 6(b) show that the estimated sky localizations of the primary (blue) and the secondary (green) events could be compatible.

In Table II, we report the follow-up parameters for GW151012 and GW151226 in the original reconstruction and by isolating the primary and the secondary events: the network SNR, the correlation coefficient (defined in Sec. II A) and the chirp mass, as estimated by LALInference (PE) and by cWB [25]. When comparing the SNR of the primaries with the estimates by LALInference, we find a SNR loss of ≈10%–15%; cWB chirp mass estimates are mostly used as an indication of "chirpness" as its estimator

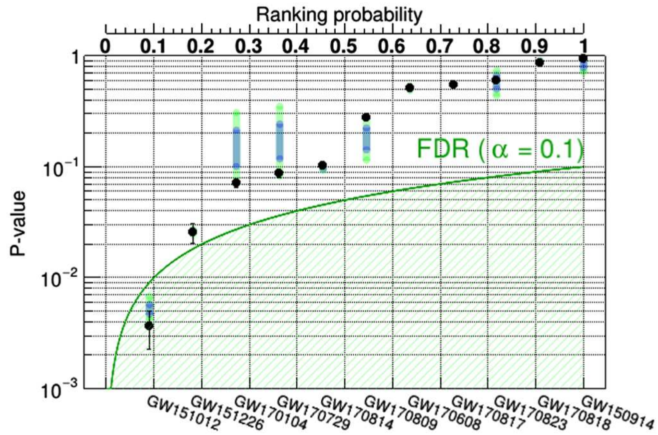

FIG. 2. Sorted p-values of the postcoalescence excesses as a function of the ranking probability (rank/N_{events}), compared with the FDR light green dashed area (with an expected fraction of false discoveries $\alpha = 0.1$). Black dots represent the minR p-values, while the blue and light green vertical lines show the 1 and 2σ [P_{sup}-P_{inf}] bounds, respectively. Out of the 11 GW events, the postcoalescence p-value$_{\mathrm{pc}}$ for GW151012 is an outlier. The second ranked event, GW151226, though mildly significant, is consistent with the 11 trials.

[5]Notice also that with the previous definition of the **w**'s, which includes a division by the amplitude spectral density in the frequency domain, this is indeed a SNR. We also note that the resulting $\mathrm{SNR}_{\mathrm{pc}}$ includes the ringdown phase of the primary signal.

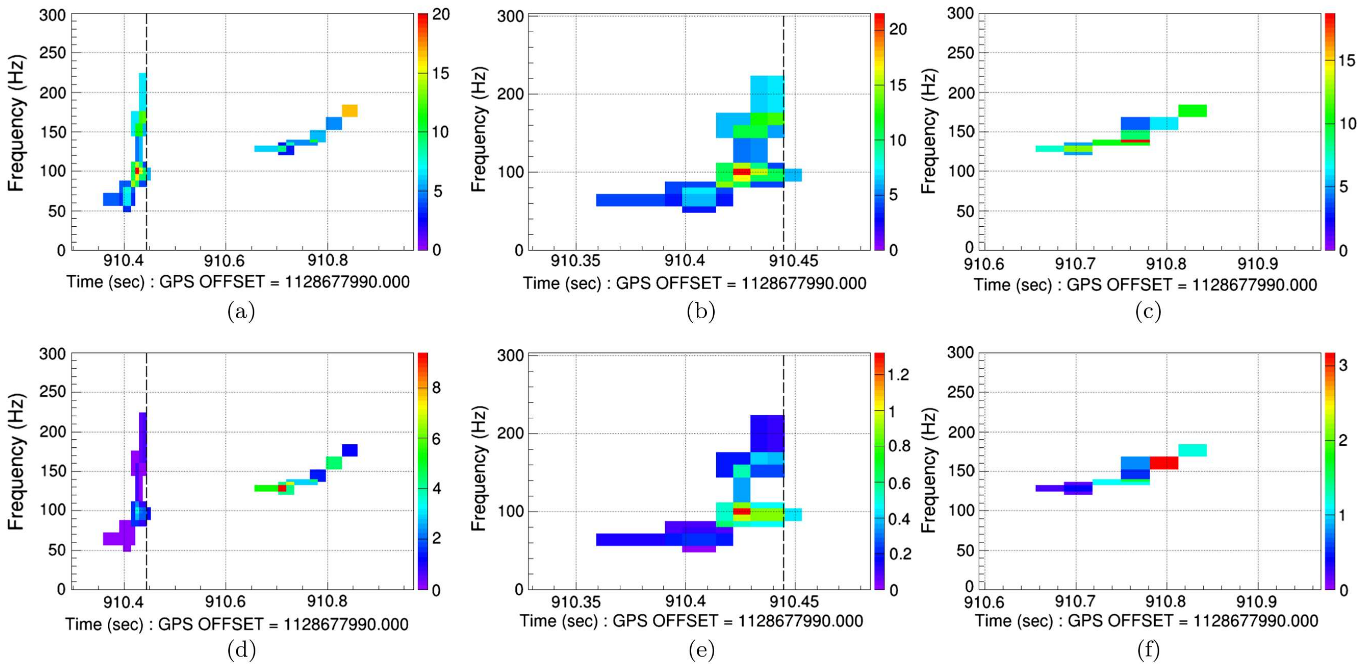

FIG. 3. cWB waveform reconstruction of GW151012, in the form of color-coded TF maps. The upper row shows the squared coherent network SNR, while the second row shows the normalized residual noise energy, E_N, estimated after the reconstructed signal is subtracted from the data. The first column [(a) and (d)] refers to the original reconstruction, with the primary chirp on the left matching the CBC PE reconstruction and a secondary cluster occurring 200 ms after the merger; an *ad hoc* time veto covering the secondary cluster was used to produce our best estimate for the GW151012 primary event shown in the second column [(b) and (e)]; finally, the third column [(c) and (f)] reports the independent reconstruction of the secondary cluster by vetoing the primary event. The dashed vertical lines denote the minR $t_{\mathrm{L,coa}}$ for GW151012 (the network reconstruction uses the Livingston detector time as a reference).

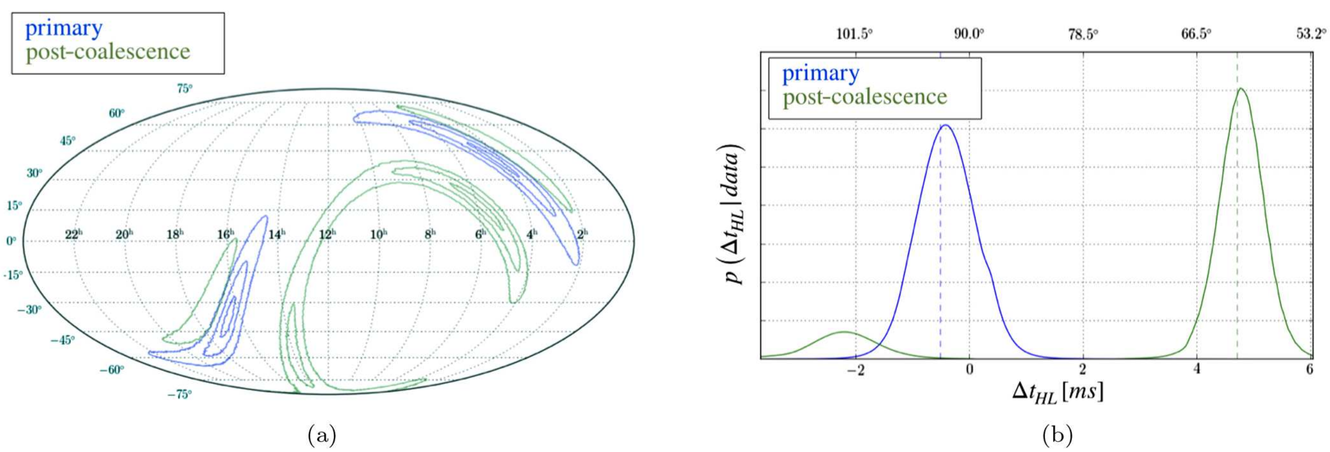

FIG. 4. (a) Mollweide projection of GW151012 primary event (blue contour lines) and the secondary event (green lines) sky reconstructions in equatorial coordinates. (b) Time delay maximum *a posteriori* probability marginals between H and L in the line-of-sight frame defined by H and L. Both figures have been produced using the code in [24].

relies on simplified assumptions that can lead to relatively large biases.

IV. DISCUSSION

In this paragraph we focus on the two outliers of the distribution of postcoalescence features from Table I, GW151012 and GW151226. The p-values are too large to exclude the null hypothesis, and yet it is useful to consider alternative explanations to exemplify the kind of findings that could be borne out of our methodology.

A. GW151012

A first plausible interpretation for the primary and secondary events in the cWB reconstruction of GW151012 is

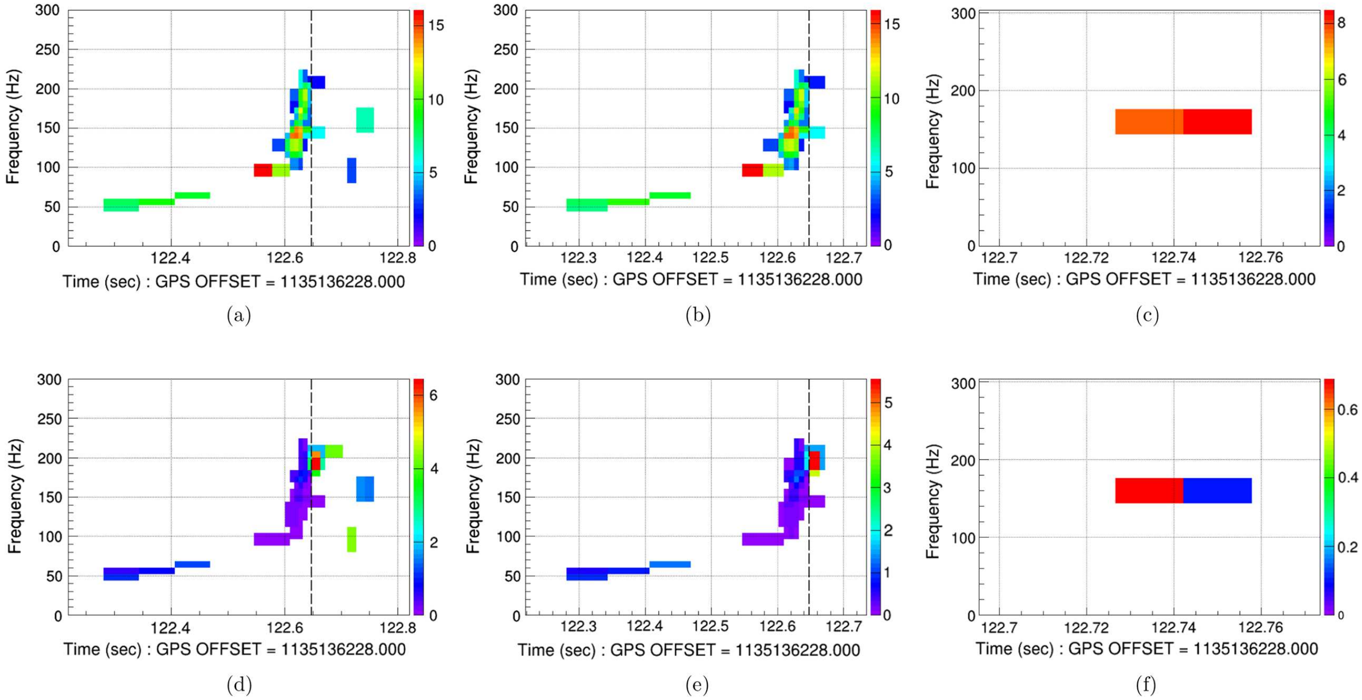

FIG. 5. cWB waveform reconstruction of GW151226, in the form of color-coded TF maps. The upper row shows the square coherent network SNR, while the second row shows the normalized residual noise energy, E_N, estimated after the reconstructed signal is subtracted from the data. The first column [(a) and (d)] refers to the original reconstruction, with the primary chirp on the left matching the CBC PE reconstruction and a secondary cluster occurring 100 ms after the merger. An *ad hoc* time veto covering the secondary cluster was used to produce our best estimate for the GW151226 primary event shown in the second column [(b) and (e)]. Finally, the third column [(c) and (f)] reports the independent reconstruction of the secondary cluster by vetoing the primary event. The dashed vertical lines show the minR $t_{\mathrm{L,coa}}$ for GW151226 (the network reconstruction uses the Livingston detector time as a reference).

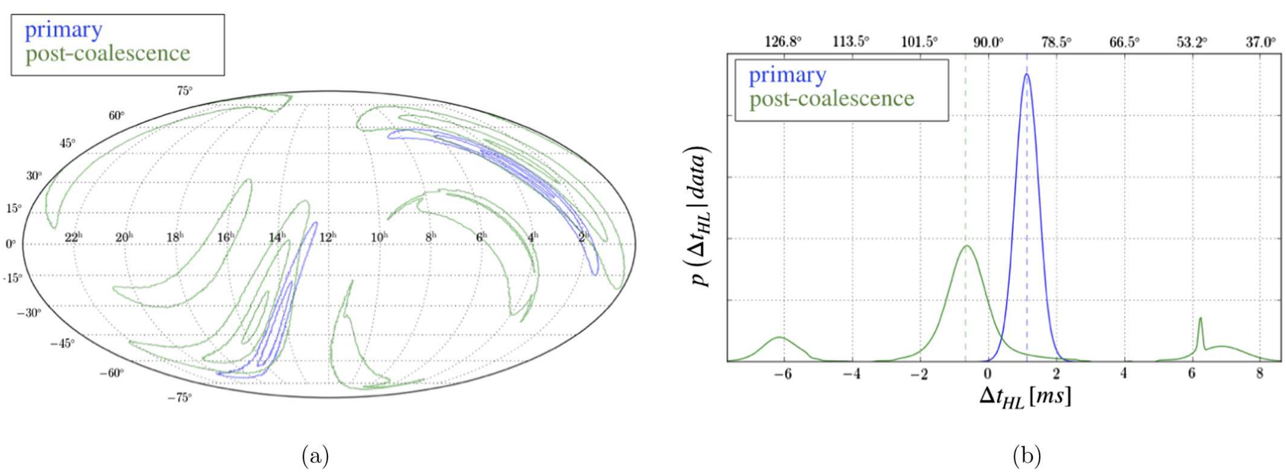

FIG. 6. (a) Mollweide projection of GW151226 primary event (blue contour lines) and the secondary event (green lines) sky reconstructions in equatorial coordinates. (b) Time delay maximum *a posteriori* probability marginals between H and L in the line-of-sight frame defined by H and L. Both figures have been produced using the code in [24].

that their occurrence may be due to an accidental coincidence of unrelated CBC events of different chirp masses and directions, compatible with catalogs of subthreshold CBC candidates; see in particular the first Open Gravitational-Wave Catalog, 1-OGC [21]. While the primary component is a well-established CBC detection, the secondary feature on its own is much fainter and it is likely originated by coherent noise from the detectors. In any case, even assuming an astrophysical origin for the secondary, according to our morphological analysis the two GWs would be unrelated.

TABLE II. Follow-up parameters for GW151012 and GW151226: the network SNR, the correlation coefficient (defined in Sec. II A) and the chirp mass as estimated by LALInference (PE) and by cWB in the original reconstruction and by isolating the primary and the secondary events.

	SNR				cc			Chirp mass ($M_\odot$)			
GW event	PE	Original	Primary	Secondary	Original	Primary	Secondary	PE	Original	Primary	Secondary
GW151012	10.0	10.5	8.4	7.1	0.81	0.95	0.83	15.2	23.8	23.8	3.2
GW151226	13.1	11.9	11.4	4.0	0.82	0.85	0.86	8.9	10.4	10.4	…

The secondary feature shows traits which are consistent with the CBC subthreshold candidates in the 1-OGC catalog [21], both morphologically and in terms of signal amplitude. In fact, its morphology is consistent with a coalescence of a light stellar mass binary, within the parameter space included by the template bank of the 1-OGC search. Also the SNR values collected at each detector by cWB are larger than 4, the threshold used for 1-OGC, and the network SNR recovered by cWB is very close to the mode of the SNR distribution of the subthreshold events in 1-OGC.[6] We expect the SNR collected by cWB to be statistically comparable with the one collected by CBC matched filter searches. This is tested for the detections described in the GWTC-1 catalog [1], and we expect it to hold also at the fainter amplitudes comparable to the secondary. The secondary feature was not found in the 1-OGC search for subthreshold CBC candidates probably because of the dead time set around all reconstructed events, such as the primary signal [21].

The rate of occurrence of subthreshold CBC candidates in 1-OGC is ~0.06 Hz, estimated from the total counts of candidates divided by the net observation time after accounting for the dead time around each selected candidate. cWB clusters together two signals if their time separation is less than 0.2 s, which corresponds to opening a time window of variable width after the coalescence time, depending on the actual duration of each signal component. In the case of GW151012, the typical time window ranges from 0.25 s for faint BBH-like secondaries to 0.37 s for faint BNS-like secondary. Therefore, the probability of random occurrence after coalescence of a subthreshold 1-OGC event within the cWB window ranges from 1.4% to 2.1% during the O1 run. Assuming similar rates for the subthreshold events in the O2 run, the order of magnitude of this probability is high enough to allow the possible occurrence of a CBC-like secondary in one out of the 11 regions after coalescence tested here. On the other hand, this probability is low enough not to be inconsistent with the measured p-value of GW151012, taking into account the uncertainties on the detection efficiency loss of cWB for candidates of the class of the 1-OGC candidates after the primary coalescence. Therefore we conclude that the secondary feature has a plausible interpretation as an object of the class of the subthreshold CBC candidates, which in turn have a population dominated by coherent noise fluctuations.

Our morphological analysis strongly disfavors any interpretation of the postcoalescence feature that is directly related to the detected GW151012, because of the inconsistency in the delay times at the detectors, which call for a different source position. In particular, this analysis disfavors alternative interpretations as postmerger echoes (see the review [26] and previous analyses in [27,28]), despite an apparent agreement in the delay time from merger and amplitude. In addition, the reconstructed spectral content does not fit the proposed echo models.

B. GW151226

The p-value of the postcoalescence feature is only marginally interesting in our analysis, and the preferred interpretation is the null hypothesis. Here, the alternative, though statistically disfavored, interpretation for the postcoalescence feature (a single tone at ~160 Hz with total duration ~0.03 s delayed by ~0.1 s) could be a fainter repetition of the merger. This would not be in contradiction with e.g., microlensing of the GW primary event or GW echoes. Microlensing could explain the observed delay time, corresponding to a fractional travel time of $\sim 2 \times 10^{-18}$, though it would require characteristics and position of the lens which appear highly unlikely from back-of-the-envelope estimations, further favoring the simpler null hypothesis. Our result also does not support echoes with respect to the null hypothesis, in agreement with previous targeted searches analyzing GW151226 and specifically aimed at echoes (see e.g., [27–30]).

C. Other GWTC-1 GWs

The standard cWB analysis of all other GWTC-1 events does not show any significant deviation from the null hypothesis in the postcoalescence tests, as reported in Table I. However, our standard setting constrains signal clustering to a time window smaller than ~0.3 s, which is not sufficient to capture the echo signal claimed for GW150914 and GW170817 in [27,31]. Motivated by those studies, we decided to expand up to 5 s the on-source time window allowed for signal clustering in the cWB analysis.

[6]The secondary feature calls for a mass ratio of the binary component significantly different from 1, from simplified matched filter analyses.

In the case of GW150914, this extension results in the appearance of an on-source postmerger event with null coherent SNR and nonzero incoherent energy; therefore we can conclude that there is no support for any signal coming from a direction consistent with GW150914.

In the case of GW170817, this extension shows a short burst of ~ 0.01 s duration and frequency ~ 130 Hz at a delay of ~ 1 s with coherent and incoherent components. By repeating the same experiment off source, the p-value of the coherent on-source SNR in the postcoalescence is about 20%, which confirms the null hypothesis. The morphology of the cWB feature is compatible with the first harmonic of the signal claimed in [31]; however, when compared with the widest class of possible postmerger events, as we do here, its p-value becomes uninteresting.

These results are insufficient to either invalidate or confirm the echo model of [31]: in fact, to be able to compare quantitatively the sensitivity of this analysis with the template searches for echoes, we would need to calibrate the detection efficiency of the cWB analysis for that specific signal class, which is beyond the scope of the present paper.

V. CONCLUSIONS

The CBC waveforms used in PyCBC, GstLAL and other similar pipelines [11] are the result of sophisticated calculations with a well-defined set of physical assumptions. The methodology discussed in this work is aimed at complementing the template-based pipelines and detecting additional features that may show up in the observed TF data as localized excesses of coherent SNR across the network. Indeed, any significant excess coherent energy can indicate the presence of astrophysical structures that reshape the theoretical waveform or point to some still unobserved physics.

Our analysis of the events in the GWTC-1 catalog [1] identifies distinct features after coalescence in the events GW151012 and GW151226 with a statistical significance which is insufficient to make any claim about their astrophysical origin, but that calls for further investigations of similar event structures in current and future observing runs. In this work, we studied the morphology of these features to search for plausible explanations, alternative to the null hypothesis. We look forward to applying this analysis to the larger set of upcoming compact binary coalescences which will be detected in the current observing run of the LIGO-Virgo Collaboration. In fact, it is very likely that the ongoing O3 run will deliver more than five times the number of gravitational events present in GWTC-1.[7]

[7]This is extrapolated from the public alerts issued in the initial part of O3. In addition, it is expected that offline analyses will identify more compact binary coalescence events than the low-latency pipelines.

In the case of GW151012, the secondary feature is consistent with a subthreshold candidate of a compact binary coalescence. Both its apparent chirpmass and apparent sky direction are different from those of the primary CBC GW signal, which seems to indicate that the secondary event is unrelated to the primary and may plausibly be due to the accidental coincidence of a subthreshold CBC candidate with the primary event.

In the case of GW151226, the morphology of the feature that appears after coalescence may suggest a postmerger phenomenon related to the detected GW, also in view of the near superposition of sky localization probability distributions. Again, we interpret this as a simple noise fluctuation.

We will be able to check if these additional features are genuine by measuring how frequently these types of outliers will occur in the O3 observation run. If the postcoalescence features of GW151012 or GW151226 are not due to simple noise fluctuations, we should have about $n = 6$ outliers similar to the one in Fig. 2 with a 10% false discovery rate. The probability that all the n outliers can be explained by noise fluctuations alone in the measurement procedure (null hypothesis) would then become extremely small, i.e,. smaller than about 10^{-n}. This shows the great importance of the false discovery rate in future analyses to test the significance of a population of outliers, as shown by several astrophysical searches [23].

We conclude by remarking that we have established a new general methodology in the framework of cWB, that can be extended to search for a larger variety of additional features, not currently included in the CBC models. In the future, we plan to widen our statistical tests to other regions of the time-frequency representation and to appraise the sensitivity of the analysis for selected models of astrophysical phenomena.

ACKNOWLEDGMENTS

The authors would like to thank Ik Siong Heng for his constructive input. We also acknowledge useful discussions with Jahed Abedi, Marco Cavaglia, Tom Dent, Sudarshan Ghonge and Tyson Littenberg. This research has made use of data, software and/or web tools obtained from the Gravitational Wave Open Science Center, a service of LIGO Laboratory, the LIGO Scientific Collaboration and the Virgo Collaboration. The work by S. T. was supported by SNSF Grant No. 200020_182047. Finally, we gratefully acknowledge the support of the State of Niedersachsen/Germany and the NSF for provision of computational resources.

APPENDIX A: cWB SKY LOCALIZATIONS FOR GW EVENTS WITHIN GWTC – 1

The reconstructed sky locations of the gravitational wave events are reported in Fig. 7. Plots show the 10%, 50% and

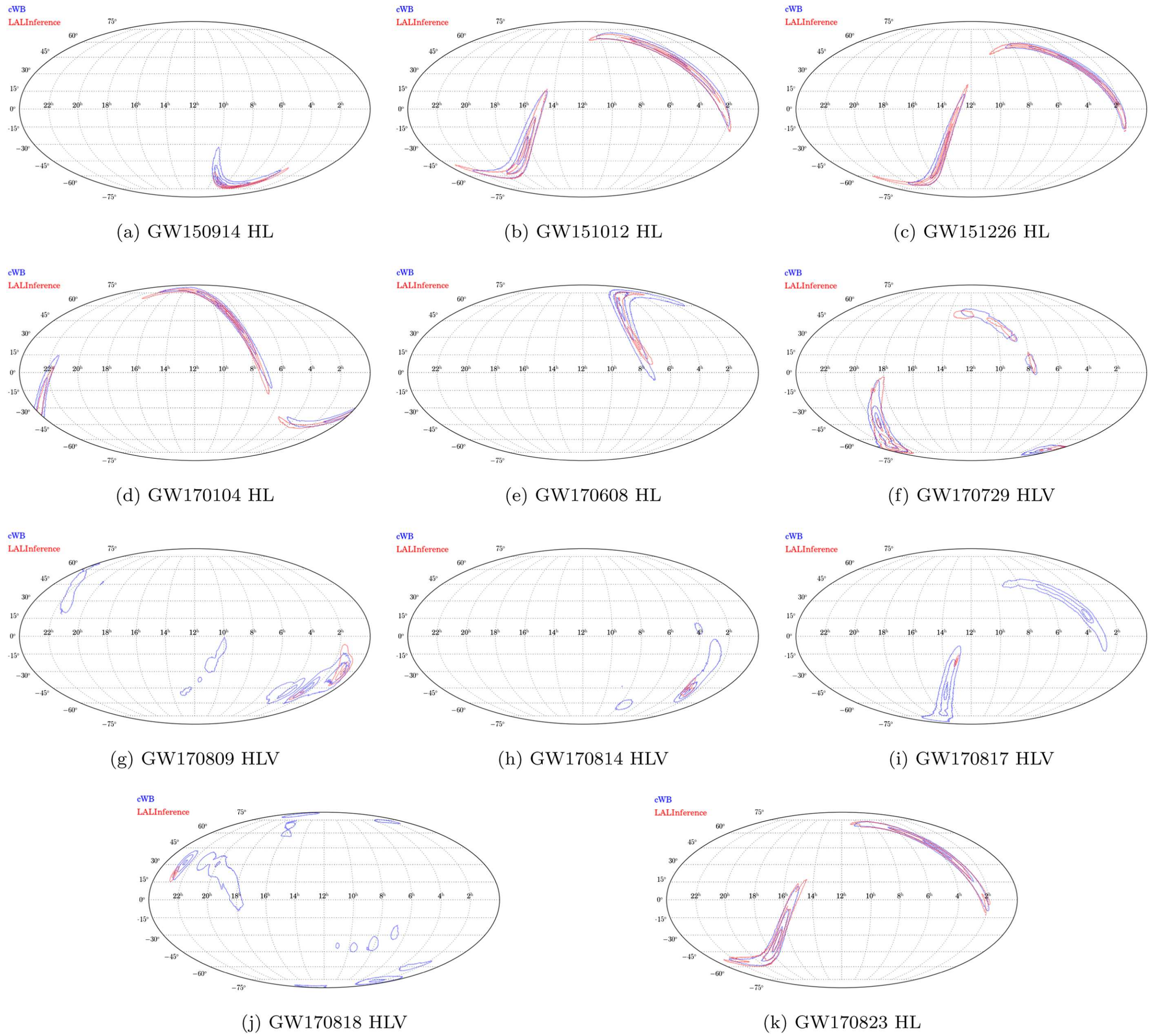

(a) GW150914 HL (b) GW151012 HL (c) GW151226 HL
(d) GW170104 HL (e) GW170608 HL (f) GW170729 HLV
(g) GW170809 HLV (h) GW170814 HLV (i) GW170817 HLV
(j) GW170818 HLV (k) GW170823 HL

FIG. 7. Mollweide projection of 10%, 50% and 90% credible regions for the sky locations of all 11 GW events in GWTC-1 [from (a) to (k)] as estimated by cWB and LALInference, in equatorial coordinates. For five GW events, i.e., GW170729, GW170809, GW170814, GW170817 and GW170818, the localizations can benefit from the data from a third site, i.e., Virgo. All the figures have been produced using the code in [24].

90% credible regions obtained from cWB (blue) and LALInference (green).[8] For five events the inclusion of the Virgo detector naturally reduces the overall area of the credible regions for both algorithms. In Table III, we report the areas of the 50% and 90% credible regions for cWB and LALInference, together with the extension of the overlapping area between the two estimates. The last two columns report the nominal probability estimated by the two algorithms when we restrict the integration inside this overlap area. Generally the results show that there is a dominant overlap when only two detectors are considered, while the modeled reconstruction has considerably reduced overlap with respect to the unmodeled one when Virgo is added in the network.

[8]Sky localization probability maps release page for GWTC-1: https://dcc.ligo.org/LIGO-P1800381/public.

TABLE III. For each of the GW events, we report a comparison between cWB and LALInference (CBC) reconstructed sky localizations: 50% and 90% sky areas with their overlap are reported. In the last two columns, we give the nominal probability as estimated by cWB and LALInference integrated over the overlap area. For five GW events, i.e., GW170729, GW170809, GW170814, GW170817 and GW170818, the localizations benefit from the data from a third site, the Virgo interferometer.

				Sky area (degrees^2)			P(overlap)	
GW event	Source	Network	CR	cWB	CBC	Overlap	cWB	CBC
GW150914	BBH	HL	50%	135	52	5	0.013	0.042
			90%	447	180	111	0.230	0.627
GW151012	BBH	HL	50%	628	436	308	0.245	0.380
			90%	2196	1555	1470	0.682	0.882
GW151226	BBH	HL	50%	420	342	185	0.218	0.267
			90%	1394	1033	902	0.659	0.841
GW170104	BBH	HL	50%	437	205	144	0.191	0.370
			90%	1399	924	712	0.612	0.783
GW170608	BBH	HL	50%	286	100	23	0.035	0.087
			90%	1067	396	346	0.482	0.818
GW170729	BBH	HLV	50%	297	143	83	0.142	0.231
			90%	1477	1033	862	0.703	0.842
GW170809	BBH	HLV	50%	299	71	52	0.082	0.390
			90%	1748	340	250	0.268	0.793
GW170814	BBH	HLV	50%	77	16	6	0.029	0.180
			90%	672	87	78	0.378	0.859
GW170817	BNS	HLV	50%	503	5	0.4	…	0.036
			90%	1812	16	16	0.007	0.902
GW170818	BBH	HLV	50%	95.9	11	…	…	…
			90%	1707.8	39	19	0.008	0.440
GW170823	BBH	HL	50%	533	430	402	0.399	0.477
			90%	1635	1651	1412	0.847	0.853

APPENDIX B: IMPLEMENTATION OF THE MONTE CARLO SIMULATION

The Monte Carlo methodology described here allows for the injection of waveform models from the public parameter estimation samples released for GWTC-1 events. The samples have been injected every 150 s in the O1-O2 data around each GW event, corresponding to roughly 5 days of interferometer coincident time including the GW trigger, with the aim of achieving at least 1000 reconstructions for each GW event. For the BBH systems this procedure employs the IMRPhenomPv2 waveform family [32–34], a phenomenological waveform family that models signal from the inspiral, merger, and ringdown phases taking into account spin effects, and including simple precession, whereas effects of subdominant (nonquadrupole) modes are not included. For the BNS system the model IMRPhenomPv2_NRTidal is used instead [35,36]; this model includes numerical relativity (NR) tuned tidal effects, as well as the spin-induced quadrupole moment.

The cWB unmodeled algorithm is applied to recover the injections, using the same settings of parameters used for O2 analysis, including the veto due to the quality of the data. All the point estimated reconstructions are used to build empirical distribution of reconstructed signals. This methodology allows us to obtain a marginalization over the posterior distribution of the models and to estimate a possible bias due to non-Gaussian noise fluctuations in a time span that covers the selected event.

[1] B. P. Abbott *et al.* (LIGO Scientific and Virgo Collaborations), GWTC-1: A gravitational-wave transient catalog of compact binary mergers observed by LIGO and Virgo during the first and second observing runs, arXiv:1811.12907.

[2] B. P. Abbott *et al.* (LIGO Scientific and Virgo Collaborations), Tests of general relativity with the binary black hole signals from the LIGO-Virgo catalog GWTC-1, arXiv:1903.04467.

[3] J. Aasi et al. (LIGO Scientific Collaboration, Advanced LIGO), Advanced LIGO, Classical Quantum Gravity, **32**, 074001 (2015).

[4] F. Acernese et al. (Virgo Collaboration), Advanced Virgo: A second-generation interferometric gravitational wave detector, Classical Quantum Gravity, **32**, 024001 (2015).

[5] J. Veitch et al., Parameter estimation for compact binaries with ground-based gravitational-wave observations using the LALInference software library, Phys. Rev. D **91**, 042003 (2015).

[6] C. M. Biwer, C. D. Capano, S. De, M. Cabero, D. A. Brown, A. H. Nitz, and V. Raymond, PyCBC inference: A Python-based parameter estimation toolkit for compact binary coalescence signals, Publ. Astron. Soc. Pac. **131**, 024503 (2019).

[7] C. Cutler, T. A. Apostolatos, L. Bildsten, L. S. Finn, E. E. Flanagan, D. Kennefick, D. M. Markovic, A. Ori, E. Poisson, G. J. Sussman, and K. S. Thorne, The Last Three Minutes: Issues in Gravitational-Wave Measurements of Coalescing Compact Binaries, Phys. Rev. Lett. **70**, 2984 (1993).

[8] S. Khan, S. Husa, M. Hannam, F. Ohme, M. Pürrer, X. J. Forteza, and A. Bohè, Frequency-domain gravitational waves from nonprecessing black-hole binaries. II. A phenomenological model for the advanced detector era, Phys. Rev. D **93**, 044007 (2016).

[9] S. Khan, K. Chatziioannou, M. Hannam, and F. Ohme, Phenomenological model for the gravitational-wave signal from precessing binary black holes with two-spin effects, Phys. Rev. D **100**, 024059 (2019).

[10] J. C. Bustillo, F. Salemi, T. Dal Canton, and K. P. Jani, Sensitivity of gravitational wave searches to the full signal of intermediate-mass black hole binaries during the first observing run of Advanced LIGO, Phys. Rev. D **97**, 024016 (2018).

[11] Gravitational Wave Open Science Center, https://www.gw-openscience.org/software/.

[12] B. P. Abbott et al. (KAGRA, LIGO, and VIRGO Collaborations), Prospects for observing and localizing gravitational-wave transients with advanced LIGO, advanced Virgo and KAGRA, Living Rev. Relativity **21**, 3 (2018).

[13] S. Klimenko et al., Method for detection and reconstruction of gravitational wave transients with networks of advanced detectors, Phys. Rev. D **93**, 042004 (2016).

[14] S. Klimenko, I. Yakushin, A. Mercer, and G. Mitselmakher, Coherent method for detection of gravitational wave bursts, Classical Quantum Gravity **25**, 114029 (2008).

[15] B. P. Abbott et al. (Virgo and LIGO Scientific Collaborations), GW170104: Observation of a 50-Solar-Mass Binary Black Hole Coalescence at Redshift 0.2, Phys. Rev. Lett. **118**, 221101 (2017).

[16] B. P. Abbott et al. (Virgo and LIGO Scientific Collaborations), GW170608: Observation of a 19-solar-mass binary black hole coalescence, Astrophys. J. **851**, L35 (2017).

[17] B. P. Abbott et al. (Virgo and LIGO Scientific Collaborations), GW170814: A Three-Detector Observation of Gravitational Waves from a Binary Black Hole Coalescence, Phys. Rev. Lett. **119**, 141101 (2017).

[18] B. P. Abbott et al., Observation of Gravitational Waves from a Binary Black Hole Merger, Phys. Rev. Lett. **116**, 061102 (2016).

[19] B. P. Abbott et al., GW151226: Observation of Gravitational Waves from a 22-Solar-Mass Binary Black Hole Coalescence, Phys. Rev. Lett. **116**, 241103 (2016).

[20] B. P. Abbott et al. (LIGO Scientific and Virgo Collaborations), GW170817: Observation of Gravitational Waves from a Binary Neutron Star Inspiral, Phys. Rev. Lett. **119**, 161101 (2017).

[21] A. H. Nitz, C. Capano, A. B. Nielsen, S. Reyes, R. White, D. A. Brown, and B. Krishnan, 1-OGC: The first open gravitational-wave catalog of binary mergers from analysis of public advanced LIGO data, Astrophys. J. **872**, 195 (2019).

[22] Y. Benjamini and Y. Hochberg, Controlling the false discovery rate: A practical and powerful approach to multiple testing, J. R. Stat. Soc.: Ser. B **57**, 289 (1995).

[23] C. J. Miller, C. Genovese, R. C. Nichol, L. Wasserman, A. Connolly, D. Reichart, A. Hopkins, J. Schneider, and A. Moore, Controlling the false-discovery rate in astrophysical data analysis, Astron. J. **122**, 3492 (2001).

[24] R. Essick, Skymap_statistics, https://github.com/reedessick/skymap_statistics, Free software (GPL).

[25] V. Tiwari, S. Klimenko, V. Necula, and G. Mitselmakher, Reconstruction of chirp mass in searches for gravitational wave transients, Classical Quantum Gravity **33**, 01LT01 (2015).

[26] V. Cardoso and P. Pani, Testing the nature of dark compact objects: A status report, Living Rev. Relativity **22**, 4 (2019).

[27] J. Abedi, H. Dykaar, and N. Afshordi, Echoes from the abyss: Tentative evidence for Planck-scale structure at black hole horizons, Phys. Rev. D **96**, 082004 (2017).

[28] A. B. Nielsen, C. D. Capano, and J. Westerweck, Parameter estimation for black hole echo signals and their statistical significance, Phys. Rev. D **99**, 104012 (2019).

[29] G. Ashton, O. Birnholtz, M. Cabero, C. Capano, T. Dent, B. Krishnan, G. D. Meadors, A. B. Nielsen, A. Nitz, and J. Westerweck, Comments on: Echoes from the abyss: Evidence for Planck-scale structure at black hole horizons, arXiv:1612.05625.

[30] J. Westerweck, A. B. Nielsen, O. Fischer-Birnholtz, M. Cabero, C. Capano, T. Dent, B. Krishnan, G. Meadors, and A. H. Nitz, Low significance of evidence for black hole echoes in gravitational wave data, Phys. Rev. D **97**, 124037 (2018).

[31] J. Abedi and N. Afshordi, Echoes from the abyss: A highly spinning black hole remnant for the binary neutron star merger GW170817, arXiv:1803.10454.

[32] S. Husa, S. Khan, M. Hannam, M. Pürrer, F. Ohme, X. J. Forteza, and A. Bohé, Frequency-domain gravitational waves from nonprecessing black-hole binaries. I. New numerical waveforms and anatomy of the signal, Phys. Rev. D **93**, 044006 (2016).

[33] M. Hannam, P. Schmidt, A. Bohé, L. Haegel, S. Husa, F. Ohme, G. Pratten, and M. Pürrer, Simple Model of Complete Precessing Black-Hole-Binary Gravitational Waveforms, Phys. Rev. Lett. **113**, 151101 (2014).

[34] P. Schmidt, F. Ohme, and M. Hannam, Towards models of gravitational waveforms from generic binaries II: Modelling precession effects with a single effective precession parameter, Phys. Rev. D **91**, 024043 (2015).

[35] T. Dietrich, S. Bernuzzi, and W. Tichy, Closed-form tidal approximants for binary neutron star gravitational waveforms constructed from high-resolution numerical relativity simulations, Phys. Rev. D **96**, 121501 (2017).

[36] T. Dietrich, S. Khan, R. Dudi, S. J. Kapadia, P. Kumar, A. Nagar, F. Ohme, F. Pannarale, A. Samajdar, S. Bernuzzi, G. Carullo, W. Del Pozzo, M. Haney, C. Markakis, M. Pürrer, G. Riemenschneider, Y. E. Setyawati, K. W. Tsang, and C. Van Den Broeck, Matter imprints in waveform models for neutron star binaries: Tidal and self-spin effects, Phys. Rev. D **99**, 024029 (2019).